New In Situ Aerosol Hyperspectral Optical Measurements over 300-700 nm, Part 1: Spectral Aerosol Extinction (SpEx) Instrument Field Validation during the KORUS-OC cruise

Carolyn E. Jordan[1,2], Ryan M. Stauffer[3], Brian T. Lamb[4], Charles H. Hudgins[2], Kenneth L. Thornhill[2,5],
5 Gregory L. Schuster[2], Richard H. Moore[2], Ewan C. Crosbie[2,5], Edward L. Winstead[2,5], Bruce E. Anderson[2],
Robert F. Martin[2], Michael A. Shook[2], Luke D. Ziemba[2], Andreas J. Beyersdorf[2,6], Claire E. Robinson[2,5],
Chelsea A. Corr[2,7]and Maria A. Tzortziou[3,4]

[1]National Institute of Aerospace, Hampton, Virginia, United States of America
[2]NASA Langley Research Center, Hampton, Virginia, United States of America
10 [3]NASA Goddard Space Flight Center, Greenbelt, Maryland, United States of America
[4]City University of New York, New York, New York, United States of America
[5]Science Systems and Applications Inc., Hampton, Virginia, United States of America
[6]California State University, San Bernardino, California, United States of America
[7]Springfield College, Springfield, Massachusetts, United States of America

15 *Correspondence to*: C. E. Jordan (Carolyn.Jordan@nasa.gov)

Abstract. In situ observations of spectrally-resolved aerosol extinction coefficients (300-700 nm at ~0.8 nm resolution) from the May-June 2016 Korea U.S. – Ocean Color (KORUS-OC) oceanographic field campaign are reported. Measurements were made with the custom-built Spectral Aerosol Extinction (SpEx) instrument that previously has been characterized only using laboratory-generated aerosols of known size and composition. Here, the performance of SpEx under realistic operating conditions in the field was assessed by comparison to extinction coefficients derived from commercial instruments that measured scattering and filter-based absorption coefficients at three discrete visible wavelengths. Good agreement was found between these two sets of extinction coefficients with slopes near unity for all 3 wavelengths within the SpEx measurement error (± 5 Mm^{-1}). The meteorological conditions encountered during the cruise fostered diverse ambient aerosol populations with varying sizes and composition at concentrations spanning two orders of magnitude. The sampling inlet had a 50% size cut of 1.3 µm diameter particles such that the in situ aerosol sampling suite deployed aboard ship measured fine mode aerosols only. The extensive hyperspectral extinction data set acquired revealed that nearly all measured spectra exhibited curvature in logarithmic space, such that Ångström exponent (α) power law fits led to large errors compared to measured values, especially in the ultraviolet (UV) wavelength range. This problem was particularly acute for α values calculated over only visible wavelengths, then extrapolated to the UV, highlighting the need for measurements in this wavelength range. Second-order polynomial fits to the logarithmically-transformed data provided a much better fit to the measured spectra than the linear fits of power laws. Building on previous studies that used total column AOD observations to examine the information content of spectral curvature, the relationship between α and the second order polynomial fit coefficients (a_1 and a_2) was shown to depend on the characteristic wavelength (λ_{ch}) of any given spectral measurement, such that differing curvature among aerosol size distributions with the same α will map to a line in (a_1,a_2) space with a slope related to λ_{ch}. Thus, spectral curvature represented by (a_1,a_2) may provide more detailed aerosol size distribution information than α alone.

1 Introduction

Significant natural variability in the size and composition of atmospheric aerosols introduces uncertainty into the representation of their optical properties and radiative impacts in models and satellite retrievals. While numerous airborne and surface-based observations over past decades have placed important constraints on these relationships, measurements have been typically limited to only one or a few wavelengths of light, which are extrapolated across the ultraviolet (UV)-visible-infrared (IR) spectrum by assuming a power law relationship (e.g., the well-known Ångström exponent). However, there is long standing evidence that extinction and aerosol optical depth spectra in the ambient atmosphere exhibit curvature that is not fully captured by a power law (e.g., King and Byrne, 1976; King et al., 1978; Kaufman, 1993; Reid et al., 1999; Eck et al., 1999, 2001a, b, 2003a, b; O'Neill et al., 2001; Schuster et al., 2006; Kaskaoutis et al., 2010, 2011; Rao and Niranjan, 2012). This wavelength-dependence of the aerosol extinction is thought to be driven primarily by the particle size distribution with only a minor contribution from the compositionally dependent aerosol absorption (Eck et al., 2001b; Schuster et al., 2006). However, these relationships remain largely qualitative and stem from columnar remote sensing measurements and Mie theory calculations. This motivates the incorporation of recently developed, advanced instruments for measuring in situ, hyperspectral aerosol extinction into field campaigns that study the ambient atmosphere.

It is important to note that the power law assumption is empirical. Used to describe the interaction between light and aerosols (e.g. Ångström, 1989; Moosmüller and Chakrabarty, 2011),

$$p(\lambda) \ = \ \beta \, \lambda^{-\alpha} \qquad\qquad (1)$$

55 p may represent various optical parameters of interest (e.g., scattering, absorption, extinction), λ is the wavelength of light (μm),

β is p at 1 μm, and α is the Ångström exponent. One advantage of this representation is that the derivative of this relationship

produces a line in logarithmic space with a wavelength-independent slope,

$$\alpha \ = \ -\frac{d \ln p(\lambda)}{d \ln \lambda} \qquad\qquad (2)$$

Hence, from any 2 wavelengths, the Ångström exponent for the entire spectrum can be determined via

60 $$\alpha \ = \ -\frac{\ln(p(\lambda_2)/p(\lambda_1))}{\ln(\lambda_2/\lambda_1)} \qquad\qquad (3)$$

The simplicity of this representation has led to its widespread use in the aerosol and remote sensing communities due to its utility

in calculating p(λ) at wavelengths for which there isn't a direct measurement. α is sensitive to the measurement error in p(λ), such

that if multiple wavelengths are available, it is preferable to perform a linear fit using Eq. (2) than a paired wavelength calculation

as in Eq. (3). If the optical property of interest is fully described by a power law, then further spectral detail beyond several

65 wavelengths is superfluous. However, if α is not, in fact, wavelength-independent for ambient aerosols, then a hyperspectal

measurement is required to capture the actual wavelength dependence.

Previous studies have considered various aerosol properties that may influence the spectral shape (and/or variation of the Ångström

exponents calculated from different pairs of wavelengths) of ambient aerosol optical depth (AOD) such as the volume mean (or

70 effective) radius of accumulation mode aerosols, the geometric standard deviation (i.e., width) of the accumulation mode, the

volume fraction of the fine mode relative to the total aerosol population, and the absorption characteristics (i.e., composition) of

the aerosol population (e.g., Reid et al., 1999; Eck et al., 1999, 2001b; Schuster et al., 2006). The relationships identified to date

remain qualitative rather than quantitative and have been based on total atmospheric column measurements from remote sensors

and on Mie calculations. The Spectral Aerosol Extinction (SpEx) instrument (Jordan et al., 2015) allows for similar analyses to

75 be performed on ambient in situ measurements, but with greater spectral resolution (~0.8 nm) than has been available previously

from the remote-sensing studies.

Although SpEx measures a narrower wavelength range (300 - 700 nm) than some remote sensors (e.g., ground-based 9 band sun-

sky radiometers AERONET (340 - 1640 nm, Giles et al., 2019) and airborne hyperspectral sun-sky radiometer 4STAR (350 - 1750

80 nm, 2 - 3 nm resolution, LeBlanc et al., 2020)) and similar ranges to others (e.g., hyperspectral polarimeters SPEX airborne (400 -

800 nm, 2 - 3 nm resolution in intensity, Smit et al., 2019; Fu et al., 2020) and SPEXone (385 - 770 nm, 2 nm resolution in intensity,

Hasekamp et al., 2019) planned for the upcoming PACE mission (Werdell, et al., 2019; Remer et al., 2019a, 2019b)), it measures

deeper into the UV range. Similar in situ instruments, such as broadband cavity-enhanced spectroscopy (BBCES) instruments

(e.g., Washenfelder et al., 2013, 2015; Bluvshtein et al., 2016, 2017; He et al., 2018), do not provide as broad a UV-visible range

85 as SpEx. Hence, SpEx is particularly suited to examine spectral details for ambient aerosols over its measurement range.

Previous work described SpEx using a series of laboratory tests that included a variety of non-absorbing and absorbing aerosols to

characterize the instrument (Jordan et al., 2015). However, the purpose of SpEx is to measure atmospheric aerosols in the ambient

environment. Hence, this manuscript is the first to offer details on the instrument performance in the field. The data presented

90 here were obtained during the Korea United States - Ocean Color (KORUS-OC) oceanographic field campaign conducted around

the Korean peninsula under the leadership of the Korean Institute of Ocean Science and Technology (KIOST) and the U.S. National Aeronautics and Space Administration (NASA). The KORUS-OC cruise was affiliated with the airborne KORUS - Air Quality (KORUS-AQ) campaign and the KOrean Coastal water Ocean and Atmosphere (KOCOA) field campaign. These joint missions were conducted to study South Korean air quality and ocean color within the field of view of South Korea's Geostationary Ocean

95 Color Imager (GOCI) that provided hourly ocean color and aerosol optical depth (AOD) measurements. Although the primary scientific objectives of the KORUS-OC cruise focused on ocean color measurements (both in situ and remotely sensed), there were also objectives to address atmospheric correction requirements and to explore interdisciplinary science questions (e.g., Tzortziou et al., 2018; Thompson et al., 2019). The joint S. Korean and U.S. based science teams sailed aboard the KIOST research vessel *R/V Onnuri* (Fig. S1). Details on the scientific objectives of these field campaigns are provided in two white papers: Al Saadi et

100 al. (2015) and US-Korean Steering Group (2015).

Two commercial instruments were also deployed to measure in situ aerosols at three visible wavelengths providing scattering coefficients and absorption coefficients. These measurements are presented in detail here and used to evaluate the performance of SpEx. Filter samples were also collected and analyzed in the laboratory for spectral absorption and chemical composition as

105 discussed in Part 2 of this work. Those data provide additional context for the measurements described here in Part 1. Further, Part 2 presents an assessment of the applicability of a methodology routinely used by the ocean color community to measure hyperspectral particle absorption for use with ambient atmospheric aerosol samples. Hence, Part 2 includes further discussion of the ability of power laws to fully represent the observed hyperspectral variability of in situ aerosol optical properties as measured during KORUS-OC.

110 2 Methods

2.1 Ship deployment

The measurements reported here from 20:25 May 21 through 09:00 June 4, 2016 Korean Standard Time (KST, KST = UTC + 9) were made outside of South Korea's territorial seas (> 12 nautical miles, 22.2 km, from the coast, Fig. 1, top left panel). The measurement package was deployed above the bridge strapped to the starboard rail in a custom-built box designed to keep the

115 instruments dry yet ventilated to prevent overheating (Fig. S1). The pumps were located in a separate box a few meters away tied to the stern rail (Fig. S1) to limit thermal and mechanical interference with the measurements. Measurements were made at ambient temperature (T), pressure (P), and relative humidity (RH), with the exception of the TAP instrument which is internally heated and kept at a constant 35 °C. T, P, and RH were measured both aboard ship and within the sampling system. Although the sampling box was ventilated, it was not climate controlled. On the top deck it was in direct sunlight during the day and even at night various

120 components in the system kept the interior warmer and drier than ambient air. These conditions led to diurnal variability in the difference between sampling and ambient conditions, such that the sampling T was ~ 6 °C warmer at night increasing to as much as ~15 °C warmer in mid-afternoon. Similarly, ambient RH ranged from 55 - 98% RH throughout the cruise, while the sampling RH ranged from ~ 30 - 70%. For the purposes of this work (both Parts 1 and 2), the comparisons made are all within this sampling system with T and RH consistent across all measurements, except for TAP. Since non-volatile black carbon (BC) is expected to

125 dominate the absorption measurement, this difference is expected to have a limited impact on the results. Hence, all data are reported here at sampling T and RH.

The available berths aboard ship constrained the number of personnel available to operate the sampling system, so it was necessary to configure the system to operate nearly autonomously. To ensure that water did not enter the sampling line, a tall stainless steel
130   sampling mast (19.05 mm (3/4") inner diameter tubing) was used to minimize the chance of sea spray entering the line from below. Further, the inlet was attached to the vertical sampling mast with a curved section of stainless steel tubing such that the inlet was downward facing to prevent any potential precipitation from entering the line from above as well (Fig. S1). This configuration worked as intended with the inlet approximately 10 m above the sea surface. However, the fast flow rate required for the SpEx measurement (approximately 70 lpm) through the curved inlet resulted in the removal of coarse aerosol with a 50% size cut of
135   ~1.3 μm diameter (Fig. S2). Hence, all of the measurements here (sampling off the same inlet line) reflect only the fine fraction aerosol in the marine boundary layer (MBL).

While the SpEx and commercial instruments were run mostly uninterrupted, colleagues from other groups aboard ship carried out the routine filter changes needed throughout the cruise. They also ensured that the system ran properly and were there to handle
140   problems, especially at the end of the cruise when the instrument box came loose and lost power in stormy weather with rough seas on the morning of June 4th. As the ship was on its way back to port and rain limited the value of restarting the system, measurements from this suite of instruments ended at that time. The methodology and results of the filter sampling will be presented in the companion paper (Part 2, Jordan et al., 2020b).

2.2 Aerosol scattering and absorption coefficient measurements and derived parameters

145   Two commercial instruments with high temporal resolution were deployed with two objectives: 1) to identify and flag incidents of ship exhaust ("plume") contamination of the data set, and 2) to evaluate the new spectral measurements (both from SpEx and the filters). The instruments deployed for this purpose were Brechtel's Tricolor Absorption Photometer (TAP model 2901; https://www.brechtel.com/products-item/tricolor-absorption-photometer, Hayward, CA) with 1 s measurement resolution at 467, 528, and 652 nm and AirPhoton's Integrating Nephelometer model 101 (IN101; https://www.airphoton.com/nephelometers.html,
150   Baltimore, MD) with ~10 s resolution at 450, 532, and 632 nm.

To identify ship plume interceptions, an initial examination of the IN101 scattering coefficient (σ_{scat}) and TAP absorption coefficient (σ_{abs}) data was performed. One-minute averages were calculated in order to calculate the single scattering albedo ($\omega = \sigma_{scat} / (\sigma_{scat} + \sigma_{abs})$). The σ_{scat} data was corrected using the submicron factors in Anderson and Ogren (1998). These corrections are
155   needed to resolve truncation errors in the forward scattering (the 7° to 0° range missing from the measurement) and non-Lambertian errors that arise from the distribution of light by the opal glass diffusor. Due to limited personnel, calibrations were not performed during the cruise. Pre- and post-cruise calibrations using pure CO_2 were performed in the laboratory to correct the final archived data and indicate the instrument performance was stable throughout the measurement period. The σ_{abs} data was corrected for scattering as recommended in Ogren et al. (2017).

160

Interception of the ship plume was first identified using one-minute averages of the gas-phase NO_2 and O_3 measurements (Thompson et al., 2019). The inlets for the gas-phase instruments were near, but not co-located with the aerosol inlet, so the one-minute averages of ω, σ_{abs}, and σ_{scat} were used to further assess evident ship plume interceptions in the aerosol data set. The σ_{abs} data were particularly sensitive to such interceptions exhibiting dramatic brief spikes in the otherwise smoothly varying time series
165   (compare σ_{abs} in Fig. S3 to the top panel of Fig. 2). These were easily identifiable and removed manually. The inlets for the in

situ instruments were towards the starboard bow (gas-phase on a lower deck, a few meters aft of the aerosol inlet) opposite of the ship stack pointed toward the port side stern. While underway, ship plumes did not affect the measurements, but they were encountered occasionally when on station or, as was more frequently the case, when getting underway from a stationary sampling site. The archived plume flags (= 0 for ambient air, 1 for ship plume interceptions) may be used to either remove data points affected by ship contamination or to assess ship plume contamination of filter samples (see Part 2).

In addition to the 1 min averaged σ_{scat} and σ_{abs} data reported in the KORUS-AQ data archive, averages were also calculated for each 30 s SpEx sampling interval and corrected in the same manner as the 1 min data set. The IN101 and TAP instruments measure at different wavelengths, so in order to calculate σ_{ext} (= σ_{scat} + σ_{abs}), the TAP data were adjusted to the IN101 wavelengths using Eq. (3). For clarity, these extinction coefficients are denoted NT σ_{ext} in comparison to the measured SpEx σ_{ext} at those wavelengths (450, 532, and 632 nm). Similarly, a second set of plume flags was created for the SpEx sampling interval (i.e., based on plume interceptions for 30 s intervals approximately every 4 minutes, see Sect. 2.3).

2.3 Spectrally-resolved aerosol extinction coefficient measurements

As described in detail in Jordan et al. (2015), SpEx is a White-type optical cell (White, 1942) with a 39.4 m path length and a 17 l internal volume. A flush time of 90 s completely exchanges the air in the cell (3 times the volume) for flow rates > 34 lpm, here, the flow rate was ~70 lpm. The optical cell is coupled via fiber optics to a UV5000 system (Cerex Monitoring Solutions, LLC, Atlanta, GA) with a 150 W xenon lamp source (Cerex P/N CRX-X150W), integrated with an Ocean Optics, Inc. (Dunedin, FL) QE65Pro 16-bit spectrometer. Sampling for 30 s using an integration time of ~20-50 ms optimizes the signal to noise ratio for each measured intensity spectrum (Jordan et al., 2015). An automated valve system controls the 4-minute sampling cycle by switching the flow between the filtered line (ambient air without aerosols) and an unfiltered line (ambient air with aerosols): 90 s flush, 30 s sample without aerosols, 90 s flush, 30 s sample with aerosols, repeat.

The intensity spectrum is measured for the sample without aerosols for a reference ($I_0(\lambda)$) and for the sample with aerosols ($I(\lambda)$) from which the extinction spectra ($\sigma_{ext}(\lambda)$) are calculated using the extinction law (Eq. (4)),

$$\sigma_{ext}(\lambda) = \frac{-ln(I(\lambda)/I_0(\lambda))}{L} \tag{4}$$

where λ is the wavelength of light and L is the optical path length (here, in units of Mm). Hence, extinction spectra are acquired every 4 minutes. Reference spectra before and after each sample spectrum are averaged together to account for drift in the intensity between measurements in the calculation of σ_{ext}. A particular strength of this measurement is it explicitly accounts for extinction arising from gas-phase constituents via the reference spectra. No calibrations are needed to obtain aerosol σ_{ext}. Laboratory tests have shown the measurement error over the full spectral range of the measurements (300-700 nm) to be about ± 5 Mm^{-1} (Jordan et al., 2015).

Several modifications have been made to the instrument since the laboratory studies reported in Jordan et al. (2015). These include an automated switching system between valves that control flow between filtered and unfiltered air and new custom control software that allows for continuous unattended operation. Further, the metal-jacketed optical fibers used previously were replaced with bare optical fibers securely packed in foam to reduce noise when deployed on mobile platforms. This last change resulted in greatly improved data quality with far fewer spectra disrupted due to mechanical disturbance under field conditions. Nonetheless,

some spectra had to be rejected from the final data set due to features that provided clear evidence of disturbance. Typically, this occurred around the times of the filter changes when the lid of the box housing the sampling system needed to be raised to change

205 filters (flagged using the plume flag field, value set to 2, see Fig. S3). Sometimes the filters were changed during flush times, leaving measured spectra unaffected, while at other times, disturbed spectra persisted for some period of time around the filter change. This suggests other vibrations arising from work involving nearby instruments or elsewhere on the ship may have contributed to the noisy rejected spectra. More work is required to further reduce the susceptibility of SpEx to sources of vibrational noise; nonetheless < 8% of the 4255 measured spectra were rejected from the data set overall. Note, ship plume interception

210 (affecting < 6% of the measured spectra) often resulted in distorted spectra likely due to rapid changes in both the aerosol population and the gas-phase concentrations used to establish the reference spectrum for the calculation of aerosol extinction as in Eq. (4). Hence, only spectra obtained when the plume flag = 0 should be used for analysis of ambient conditions.

One consequence of unattended operation is the intensity drift sometimes resulted in saturated pixels around 332 nm and 467 nm

215 due to peaks at those wavelengths in the lamp spectrum (Fig. S4). Saturation can be prevented either by adjusting the integration time of the spectrometer or by realigning the optics. However, unattended operation necessitated filtering the spectra at those two wavelengths when saturation occurred. The 16-bit spectrometer has a maximum intensity count of 65,536 (2^{16}), however, saturation effects became apparent before reaching this maximum. Tests showed that a threshold of 63,000 counts was a suitable limit for removing saturation effects from the spectrum. Filtering the 467 nm channel and the two adjacent pixels on either side

220 of that channel removed the saturation distortions completely. The saturation effects at 332 nm were filtered in the same way, however, there appeared to be a minor shoulder effect that extended over a broader wavelength range in the UV. The effect was minimal (a few percent of the measured value) and well within the measurement error. However, caution is recommended against over-interpreting the shape of a spectrum in the vicinity of 332 nm when the saturation flag (Sat332Flag) for this channel is set to 1. Saturation at 332 nm affected 16% of the total 4255 measured spectra.

225 3 Results

3.1 Overview of σ_{scat} and σ_{abs} during KORUS-OC

Four distinct synoptic meteorological regimes have been described in detail for the KORUS-AQ period (Peterson et al., 2019). The KORUS-OC cruise departed the peninsula (Fig. 1, top left panel) sailing to the East Sea (Sea of Japan) near the end of the 2nd of these periods, the Stagnant period, characterized by limited transport and enhanced photochemical production of secondary

230 organic aerosols (Kim et al., 2018; Nault et al., 2018; Choi et al., 2019; Jordan et al., 2020a). This regime started breaking down on May 23rd, followed by a precipitation event on the 24th that reduced ambient aerosols to low concentrations as reflected by low (tens of Mm^{-1}) σ_{scat} (Fig. 2, top panel).

From May 25th through the 31st the Transport/Haze period was characterized by air mass transport (from the west/northwest

235 carrying pollutants from China), overcast hazy conditions, and rapid local South Korean secondary production of inorganic aerosols resulting in the largest concentrations of the PM$_{2.5}$ fraction of aerosols (i.e., particulate matter with diameters ≤ 2.5 μm) observed during the KORUS-AQ campaign (Peterson et al., 2019; Eck et al., 2020; Jordan et al., 2020a). The greatest σ_{scat} values (hundreds of Mm^{-1}) observed aboard the R/V Onnuri were found during the first half of the Transport/ Haze period while the ship was

downwind of the Korean peninsula in the East Sea (Fig. 1, top panels, and Fig. 2, top panel). Lower σ_{scat} values were observed
240 during this period when the ship was upwind of the peninsula following its transit to the West Sea (Yellow Sea).

The final of the four synoptic periods, the Blocking period, followed a frontal passage that ended the previous Transport/Haze
period (Peterson et al., 2019). This final frontal passage swept in cleaner air from the north leading to a rapid decrease in aerosol
concentrations reflected in the reduced σ_{scat} observed aboard ship (Fig. 2). The Blocking period was then characterized by limited
245 transport and occasional brief stagnant periods, where local sources dominated pollutants, but aerosols did not accumulate to large
concentrations (Peterson et al., 2019; Jordan et al., 2020a). This led to strikingly low σ_{scat} values (tens to < 10 Mm^{-1}, Fig. 2), even
lower than those observed during the precipitation event on May 24th.

Throughout the cruise σ_{abs} values were typically an order of magnitude smaller than σ_{scat} (Fig. 2, top panel) with peak values
250 generally found at the same locations and times as peak σ_{scat} (Fig. 1). Hence, while the temporal variability of σ_{abs} largely followed
σ_{scat}, the range in the magnitude of σ_{abs} (0.36 - 18.07 Mm^{-1}) at 532 nm was far less than that of σ_{scat} (2.8 - 332.2 Mm^{-1}). This led
to the finding that single scattering albedo values ($\omega(\lambda) = \sigma_{scat}(\lambda) / \sigma_{ext}(\lambda)$) were driven by the change in scattering not absorption.
Typically, ω was > 0.9 (Fig. 1, bottom right panel, and Fig. 2, bottom panel). The excursions below this value observed on May
23rd and 24th occurred when the reduction in σ_{scat} exceeded that observed in σ_{abs}.
255

The most extreme low values of ω (~ 0.7 for 532 nm, Figs. 1 and 2), however, occurred during the Blocking period, when the
temporal evolution of σ_{abs} did not closely follow σ_{scat}. At that time, the scattering Ångström exponents (α_{scat}) increased to values
> 3, while absorption Ångström exponents (α_{abs}) were ~ 1 (Fig. 2, middle panel). These data indicate that the aerosol population
was dominated by small particles, likely black carbon (BC). The temporal evolution of carbon monoxide (CO, Fig. 2, bottom
260 panel) and σ_{scat} (Fig. 2, top panel) were strikingly similar from 04:00 June 1st through 20:00 June 2nd, exhibiting an $r^2 = 0.841$ for
a linear regression over that time. This is in contrast to the Blocking period as a whole ($r^2 = 0.514$) or the rest of the campaign,
excluding the Blocking period ($r^2 = 0.623$). The good correlation with CO, the BC signature in α_{abs}, the small particle population
indicated by α_{scat}, and the limited transport of the Blocking period, together suggest that the low ω values arose from local ship
emissions either from commercial or fishing vessels or both.
265

Aside from the Blocking period, α_{scat} typically ranged from ~ 1.5 - 2, with evident wavelength dependence in the α_{scat} wavelength
pairs (Fig. 2, middle panel). Little difference was found among the wavelength pairs in the α_{abs} values that typically ranged from
~0.5 - 1 throughout the cruise.

3.2 Comparison of SpEx data to σ_{ext} calculated from $\sigma_{scat} + \sigma_{abs}$

270 σ_{ext} calculated from the $\sigma_{scat} + \sigma_{abs}$ data (denoted NT σ_{ext} to distinguish it from SpEx σ_{ext}) averaged over the SpEx sampling intervals
(see Sect. 2.2) were compared to the 450, 532, and 632 nm channels of SpEx (Fig. 3). Excellent agreement was found with slopes
of 1.020 ± 0.002, 0.998 ± 0.003, and 1.057 ± 0.004 for all of the data in each of the three channels (gray plus markers in all panels
of Fig. 3), respectively. Three intervals were used to look at mean comparisons: 15 min (light colored circles), 30 min (dark
colored triangles), and 60 min (black diamonds). The slopes, intercepts, and r^2 values for all of the fits are shown in Fig. 3. These
275 fits were performed using data limited to the valid measurement range (i.e., above the lower limit of detection, LLOD). Tests
indicated that a limit of twice the measurement uncertainty provided a suitable LLOD (10 Mm^{-1}).

The SpEx data were more variable than the NT σ_{ext} as is evident in time series comparisons throughout the cruise (Figs. 4, S5, and S6, top panel). This is partly attributable to the differing noise characteristics of the measurement techniques, but it largely arises

280   from differences in sampling intervals. The NT σ_{ext} represent 30 s means calculated from ~10 s σ_{scat} and 1 s σ_{abs} measurements for each SpEx σ_{ext} spectrum. Averaging SpEx σ_{ext} reduces the variability (Figs. 4, S5, and S6, middle panel) according to the standard error of the means. However, not all of the variability evident in Fig. 4 is noise. Limiting the data range in the time series to 2 days (Fig. 5) illustrates that the native resolution of SpEx captured rapid changes that were also evident in the NT data. For example, consider the double peak feature that occurred around 03:00 on May 25th (top panel, Fig. 5). This temporal variation is

285   lost even in the 15 min average (bottom panel, Fig. 5).

For clarity, the standard deviations for the means are shown separately (Figs. 4, S5 and S6, bottom panels). Most of the standard deviations of the means in these channels were consistent with the measurement error of about ± 5 Mm^{-1} with larger values arising from changes in the ambient conditions. Hence, the standard deviations of the 60 min means describe an upper envelope compared

290   to the 15 and 30 min means as changing ambient conditions led to greater variability in the means. Together, the results shown in Figs. 3-5 show that quantitative data were obtained under field conditions with SpEx at its native sampling resolution.

3.3   Evaluating extinction Ångström exponents (α_{ext}) with hyperspectral extinction data

With the spectral data available from SpEx, it was possible to test the power law behavior of the individual and mean spectra by fitting a line to each spectrum in logarithmic space per Eq. (2), where the Ångström exponent, α_{ext} is the negative value of the

295   slope. As discussed in the introduction, if a power law described the relationship well, α_{ext} should be invariant with wavelength. Yet clear separation was found in α_{ext} from linear fits to all of the individual spectra (All Data, Fig. 6, left panel) depending on the wavelength range used for the fit. The α_{ext} from fits to the full range (300-700 nm), and two partial ranges (450-532 nm) and (532-632 nm) deviate from the 1:1 line expected when plotted vs. α_{ext} from fits to the 450-632 nm range. This result was also found for α_{ext} determined from all of the mean spectra sets as well (e.g., those from the 30 min mean spectra, right panel Fig. 6).

300

Most of the SpEx spectra measured during the cruise exhibited curvature over the 300-700 nm range in logarithmic space. Note, in order to compare results here to previously published work (Sect. 4), for the remainder of this section fits will be shown using wavelength in units of μm. This change in units does not alter the values of α_{ext} (which are invariant with wavelength and hence, the choice of units does not matter), but it does change the other coefficients from the mathematical fits to the spectra that will be

305   discussed. An example of the observed curvature is provided in Fig. 7. The measured spectrum shown (red curve, Fig. 7, all panels) is curved such that residuals (the difference between the measured spectrum and the mathematical fit, blue curves) from the linear fits (black lines, left panels) are also curved. If a particular mathematical function (here, a power law) provides a good fit to the data, the residuals should be randomly distributed around zero. If there is a trend (the curvature evident here), then other functions should be considered to see if a better fit may be obtained. The curvature in the residuals is evident not only across the

310   full wavelength range (Fig. 7, bottom left panel), but for subsets of that range as well (e.g., the 0.45 - 0.632 μm fit, Fig. 7, top left panel).

This wavelength dependent curvature can lead to large errors if used to extrapolate to wavelengths beyond the measured range of values. For example, using α_{ext} found from the 0.45-0.632 fit to extrapolate to 0.3 μm (Fig. 7, middle left panel) leads to a value

315 of $LN(\sigma_{ext})$ = 5.7099, while the measured value was 5.0839, i.e., an extrapolated extinction of 302 Mm^{-1}, 87% larger than the measured extinction of 161 Mm^{-1}. This wavelength is the most extreme, but the positive artifact is present throughout the UV range: with the extrapolated extinction 73% and 29% greater at 0.315 and 0.365 μm, respectively. At 0.45 μm ($LN(0.45$ μm) = -0.8, Fig. 7), the lower end of the fit range of values, the fit extinction was 6% greater than the measured value, while at 0.532 μm (the middle of the fit range) it was 3% less.

320

Previous work has shown that 2nd order polynomials in logarithmic space can provide a better fit to ambient aerosol optical depth (AOD, aerosol extinction integrated over an atmospheric column) spectra than power law fits (e.g., Eck et al., 1999, 2001a, b, 2003a, b; Schuster et al., 2006; Kaskaoutis et al., 2010, 2011). In the example shown in Fig. 7, it is clear that a 2nd order polynomial fit (black curves, right panels) reduces the trends in the residuals both over the full wavelength range (bottom right) and over the

325 0.45-0.632 μm subset of that range (top right) from that obtained from the linear fits. The improved fit provided by a 2nd order polynomial for all of the measured spectra is shown using histograms of the residuals at 6 wavelengths across the measured wavelength range (Fig. 8). For both the linear fits (black bars) and the 2nd order polynomial fits (red bars), the range of values for residuals at each wavelength is divided into 20 bins. The narrower bins for the 2nd order polynomial fits reflect the smaller range in residual values compared to those from the linear fits. The best agreement between the two sets of residuals shown in Fig. 8 is

330 found at 0.532 μm, where the linear fit residuals are distributed around zero. At longer and shorter wavelengths, however, the linear residuals tend to be either positive or negative at any given wavelength, while the 2nd order polynomial fit residuals are centered around zero across all wavelengths. These results confirm that 2nd order polynomials provide a better fit to the data than linear fits.

335 Unfortunately, just as extrapolating linear fits beyond the measurement range is problematic, the same is also true for the 2nd order polynomial fits (Fig. 7, middle right panel). In this case, at 0.45 and 0.532 μm (within the fit range) the fit agrees with the measured extinctions within 1% (~85 and 56 Mm^{-1}, respectively). However, at increasingly shorter wavelengths the fit diverges from the measured spectrum with the fit values 15%, 28%, and 34% too small at 0.365, 0.315, and 0.3 μm, respectively. The divergence of either fit from the measured spectrum when extrapolating beyond the fit wavelength range (Fig. 7, middle panels) highlights the

340 need for measurements across a broad spectral range in order to minimize the need for extrapolation.

4 Discussion

The motivation to fit the SpEx spectra with a 2nd order polynomial came primarily from the work of Schuster et al. (2006) in which both Mie calculations and AERONET data were used to explore the additional information that spectral curvature may provide. A comparison of the coefficients obtained from SpEx to those in Schuster et al. (2006) revealed two key differences between the

345 data sets. First, the a_1 and a_2 coefficients spanned a wider range of values than those obtained in the prior work (Fig. 9, top left panel). Second, Schuster et al. (2006) reported an empirical approximation such that α_{ext} was approximately equal to a_2-a_1. This approximation clearly does not hold for the values obtained from this data set (Fig. 9, top left panel). These differences can be understood as follows.

350 The two expressions used here to fit the relationship between σ_{ext} and λ are related by their negative derivative, defined as α in Eq. (2). That is, the derivative of the linear fit (y=a+bx; dy/dx = b) equals the derivative of the 2nd order polynomial fit (y = a_0 +a_1x +a_2x^2; dy/dx = a_1 +2a_2x) such that

$$\alpha_{ext} = -b = -(a_1 + 2a_2(ln(\lambda))) \qquad (5)$$

Hence, for any given spectrum, there is a wavelength at which the linear and 2nd order polynomial fits yield equivalent results.

355 This wavelength (called the characteristic wavelength, λ_{ch}) can be calculated from the two sets of fit coefficients for each spectrum. For the SpEx data set, λ_{ch} was found to range from 0.36 - 0.46 μm. In contrast, the empirical fit of $\alpha_{ext} = a_2-a_1$. implies $\lambda_{ch} \sim 0.61$, i.e., ln(0.61) ~ -0.5. The wavelength dependence of Eq. (5), results in spectra sets with differing λ_{ch} exhibiting different mapping between α_{ext} and (a_1,a_2). To illustrate this, consider the range of α_{ext} values (0.29 - 3.25) found from linear fits over 0.3 - 0.7 μm to all of the spectra measured by SpEx during KORUS-OC. This range of α_{ext} values maps differently into (a_1,a_2) space as a

360 function of λ_{ch} (Fig. 10, top right panel). There are two limiting cases where $\alpha_{ext} = a_1$: either $a_2 = 0$ (i.e., no curvature in the spectrum) or $\lambda_{ch} = 1$ μm (i.e., ln(1) = 0). The former leads to all λ_{ch} sets overlapping at $a_2 = 0$, while the latter exhibits a broad vertical band independent of curvature (a_2) (Fig. 9, top right panel).

As λ_{ch} decreases, the mapping rotates counter-clockwise occupying an increasingly narrow band in (a_1,a_2) space (Fig. 9, top right

365 panel). The angular difference between $\lambda_{ch} = 0.61$ μm and 0.41 μm accounts for the shift between the mapping reported in Schuster et al. (2006) and this work. The differing values in λ_{ch} arise from the different spectral ranges between AERONET (7 bands spanning 0.34 - 1.02 μm, Schuster et al. (2006)) versus 0.3 - 0.7 μm for SpEx. The α_{ext} values from fits to the spectra set map into the expected bands (Fig. 9, bottom panel) with the color distribution shifting slightly over the range of calculated $\lambda_{ch} = 0.36 - 0.46$ μm. Note, that the most extreme values both to the right and the left of the distribution are related to shorter λ_{ch} than the rest of

370 the data set.

Schuster et al. (2006) used this type of coefficient mapping to distinguish different aerosol size distributions via curvature that otherwise exhibit the same α. In particular, while fine mode aerosols exhibit negative curvature, the presence of sufficient coarse mode aerosols in a bimodal size distribution induces positive curvature due to the efficient extinction of light at longer wavelengths

375 by larger particles. Here, the inlet limited the size range of sampled aerosol to the submicron fraction, such that positive curvature is not expected. Aerosol size distributions were not measured aboard ship during the cruise, but as discussed in Sect. 3.1 previously published work, along with additional inferences made in that section, provide sufficient context about the types and sizes of aerosols prevalent in the region during the campaign to enable a broad assessment of the mapping of SpEx data into (a_1,a_2) space. For clarity, the 60 min mean spectra data are used (Fig. 10).

380

In addition to the evident separation in α_{ext} across (a_1,a_2) space (Fig. 9 and top left panel of Fig. 10) there is also clear separation as a function of aerosol loading using $\sigma_{ext}(0.532$ μm) as a proxy for ambient aerosol concentrations (Fig. 10, lower left panel). High concentrations ($\sigma_{ext}(0.532$ μm) > 150 Mm^{-1}) exhibit a relatively small range of a_1 and a_2 values. Generally, these spectra exhibit the greatest curvature (i.e., largest absolute values of a_2 for any given a_1). In contrast, low concentrations ($\sigma_{ext}(0.532$ μm)

385 < 75 Mm^{-1}) span a wide range of values in a_1 and a_2. As described in Sect. 3.1 there were three distinct meteorological regimes during the cruise (Peterson et al., 2019) that led to different ambient aerosol populations. Hence, the separation in aerosol loading should not be viewed as a function of loading for a uniform aerosol population, but rather as an artifact of the differing size distributions and to a lesser extent, composition.

390 The (a_1,a_2) map separated according to the defined meteorological regimes reveals strikingly different distributions for the 3 periods (Fig. 10, top right panel). The spectra during the Stagnant period (predominantly submicron aerosols, where PM$_{2.5}$ ~ PM$_1$ (Jordan

et al., 2020a), dominated by locally produced SOA (Kim et al., 2018; Nault et al., 2018; Peterson et al., 2019; Choi et al., 2019; Jordan et al., 2020a)) produced a remarkably narrow range of a_1 and a_2 values that essentially lie along a single α_{ext} line (~1.5) for the 60 min mean spectra set. In contrast, the spectra during the Blocking period (likely small absorbing aerosols from relatively fresh ship emissions) exhibit a wide range in a_1 and a_2 values with values of α_{ext} generally > 1.6. However, α_{ext} values for this group also span the full range of observed α_{ext} primarily when the absolute value of a_2 was small ($\leq$ |-0.6|). The large variability of this group may be due in part to the low extinctions where the sensitivity of α_{ext} to uncertainty in σ_{ext} is greatest. It may also reflect the heterogeneity of aerosol sources encountered in the marine boundary layer as the ship cruised around the West Sea during this period.

Finally, the period when aerosol concentrations were highest, Transport/Haze, exhibits the same range in a_1 as the Stagnant aerosols, but with greater curvature (i.e., larger absolute values of a_2, Fig. 10, top right panel). During this period the meteorological conditions that transported polluted air masses eastward from China, also created conditions that promoted rapid secondary inorganic aerosol production locally over the S. Korean peninsula (Peterson et al., 2019; Eck et al., 2020; Jordan et al., 2020a) that resulted in the growth of fine mode aerosols to larger sizes ($PM_{2.5} > PM_1$, Eck et al., 2020; Jordan et al., 2020a) than observed during the Stagnant period. During the first half of the Transport/Haze period the ship was downwind of S. Korea in the East Sea, while during the second half it was upwind in the West Sea. Splitting the data from this period to reflect the position of the ship (Fig. 10 bottom right panel) shows that the highest concentrations of aerosols were observed downwind of S. Korea and exhibited the greatest curvature and the lowest α_{ext}. This result indicates larger particle sizes were present downwind than upwind, consistent with the reported changes in aerosol size distribution due to local production over the Korean peninsula (Eck et al., 2020; Jordan et al., 2020a). The upwind distribution resembles the narrow Stagnant distribution in (a_1, a_2) space, but shifted to a slightly lower α_{ext}.

It is interesting to contrast the range in curvature between the three periods. As shown in Fig. 6, α_{ext} decreases as the fit range is extended to shorter wavelengths. This is due to the curvature evident in the UV range of Fig. 7 which is not adequately captured by fits to the longer wavelength subranges. In that instance (an individual spectrum from the Stagant period), α_{ext}(0.45-0.632 µm) = 3, whereas α_{ext}(0.3-0.7 µm) = 2.04. The greatest curvature tends to be found for the period with the largest particles observed during the campaign, while for the period when the particles were likely to be smallest, the UV curvature is small or absent leading to larger α_{ext} values (Fig. 10). In addition, the largest absolute values of a_1 ($\geq$ |-6|) found in the individual spectra (Fig. 9) arise from partial spectra where the longer wavelengths of a measured spectrum are below detection. Spectral fits were limited to only above detection portions of the measured spectrum. This is why the λ_{ch} for these spectra shift to shorter wavelengths. These spectra are those for which scattering and extinction were observed to be low, hence, the spectral fit is subject to greater uncertainty. This accounts for the finding that some of the fine fraction Blocking period aerosols, both exhibit curvature as large as the other two periods, as well as the limited negative curvature ($a_2 \leq$ |-0.5|) and in a few cases, slightly positive curvature ($a_2 \geq 0$, Figs. 9 and 10).

5 Conclusions

This work, Part 1 of 2, examined the high temporal resolution data set (IN101, TAP, and SpEx) collected as part of the in situ aerosol measurement suite deployed aboard the *R/V Onnuri* for the KORUS-OC cruise. IN101 scattering (σ_{scat}) and TAP

absorption (σ_{abs}) coefficients were measured at three visible wavelengths throughout the cruise, with single scattering albedo (ω)
430 calculated from them. These data were presented to provide an overview of the in situ aerosol measurements throughout the cruise
within the context of the prevalent meteorological regimes previously reported for the KORUS-AQ field campaign (Peterson et
al., 2019; Jordan et al., 2020a). The cruise took place during 3 distinct meteorological periods where, 1) stagnant conditions
fostered local (S. Korean) production of secondary organic aerosol, 2) transport from China coupled with local overcast and humid
hazy conditions led to secondary production of inorganic aerosol with rapid growth of fine mode aerosols to larger particle sizes,
435 and 3) a blocking period with limited transport following a frontal passage that dramatically reduced aerosol concentrations.
Results presented here suggest the aerosols observed aboard *R/V Onnuri* during this final period were likely relatively fresh small
particles from ship emissions into the marine boundary layer. The largest values of σ_{scat} and σ_{abs} were observed when the ship was
downwind of the Korean peninsula in the East Sea during the Transport/Haze period. The smallest values of ω were found when
the ship was upwind of the peninsula in the West Sea, with low values arising from reductions in scattering rather than increases
440 in absorption.

Extinction coefficients (σ_{ext}) calculated from the 3 visible wavelength σ_{scat} and σ_{abs} data were used to evaluate the performance of
SpEx under field conditions that offered a wide range of concentrations, particles sizes, and composition. Excellent agreement
was found for all 3 wavelengths with slopes equal to 1.020 ± 0.002, 0.998 ± 0.003, and 1.057 ± 0.004 with $r^2 = 0.981, 0.969$, and
445 0.942 for the 450, 532, and 632 nm channels, respectively. A lower limit of detection of 10 Mm^{-1} was determined for the individual
spectral measurements (twice the standard deviation of the measurement) that can be reduced via standard error of the means when
averaging spectra over longer sampling intervals. The broad spectral range (300 - 700 nm) and fine spectral resolution (0.8 nm)
provided an opportunity to examine the wavelength dependence of the spectra for a diverse set of in situ ambient aerosols. Nearly
all of the measured spectra exhibited curvature in logarithmic space such that 2nd order polynomials provided a better fit to the data
450 than the usual linear fit of a power law representation. With either fit, evidence was presented to highlight the large deviation of
an extrapolated value for σ_{ext} beyond the fit wavelength range. This finding highlights the need for measurements that extend well
into the UV, thereby limiting the need for extrapolated estimates of σ_{ext} in that part of the spectrum.

A comparison to a previous study of spectral curvature based on Mie calculations and remote sensing data from AERONET
455 (Schuster et al., 2006) revealed the wavelength dependence that relates the Angstrom exponent (α) to the 2nd order polynomial
coefficients (a_1 and a_2). The characteristic wavelength (λ_{ch}) of any given data set needs to be taken into account when comparing
spectral curvature coefficients across data sets. Mapping the fit coefficients shows that any given α representation can be separated
along a line in (a_1, a_2) with a slope of λ_{ch} such that spectral curvature can be used to obtain more detailed information about aerosol
size distribution. The work of Schuster et al. (2006) was directed to distinguishing different bimodal size distributions on the basis
460 of the presence of coarse fraction aerosols. Here, only fine mode aerosols were sampled, nonetheless, the separation found in
(a_1, a_2) space across the KORUS-OC data set suggests that curvature may be used to infer more detailed size distribution information
even within the fine mode alone. Size distributions were not measured aboard the *R/V Onnuri*, so such a study will require future
ambient measurements to fill this data gap.

465 In Part 2 (Jordan et al., 2020b), the methodology used for the filter analyses from the KORUS-OC in situ aerosol measurement
suite is described with an overview of the results provided. The data from those filters include total aerosol σ_{abs} spectra (300-700
nm) from glass fiber filters placed in the center of an integrating sphere, soluble aerosol absorption coefficient spectra (300-700

nm) from deionized water (σ_{DI-abs}) and methanol ($\sigma_{MeOH-abs}$) extracts of Teflon filters measured with a liquid waveguide capillary cell, water-soluble inorganic ion (WSII) concentrations via ion chromatography, and water-soluble organic compounds (WSOC)

470 that contribute to the aerosol measured using an aerosol mass spectrometer. The combination of filter-based σ_{abs} spectra (300-700 nm) with the SpEx σ_{ext} spectra set, allows for the calculation of spectral ω (300-700 nm) for in situ aerosols. Part 2 includes a similar examination of power law and 2nd order polynomial representations of all 4 of the in situ aerosol hyperspectral data sets obtained during KORUS-OC. It also explores relationships between the optical properties and water-soluble composition information within the meteorological context of KORUS-AQ following the discussion presented here in Part 1.

Data Availability

All data presented here are available under the *R/V Onnuri* Ship tab in the KORUS-AQ archive (DOI: 10.5067/Suborbital/KORUSAQ/DATA01).

Author contribution

CEJ led the experiment, analyzed the data, and wrote the manuscript.

480 CEJ, BEA, LDZ, CHH, KLT, ELW, RFM, MAS, AJB, CER built elements of the hardware, software, and deployment measurement system; and assisted in the laboratory at NASA LaRC.

CEJ, BEA, AJB, CAC participated in the field work.

RMS, BTL, & MAT deployed with the measurement suite aboard the R/V Onnuri, collected filter samples, and contributed to the manuscript.

485 GLS, RHM, LDZ, BEA, ECC, MAS, RMS, AJB, & CAC contributed to the data analysis and the manuscript.

Competing interests

The authors declare that they have no conflict of interest.

Acknowledgements

The authors gratefully acknowledge the support of the KORUS-OC and KORUS-AQ science teams, the outstanding support
490 provided by our South Korean partners at the Korean Institute for Ocean Science and Technology (KIOST), and financial support from the NASA/NIA cooperative agreement NNL09AA00A and NASA Grant NNX16AD60G through the Geostationary Coastal and Air Pollution Events (GEO-CAPE) mission pre-formulation studies. The authors particularly thank Anne Thompson for her support throughout this study and Fred Brechtel and Vanderlei Martins for helpful discussions

References

495 Al-Saadi, J., Carmichael, G., Crawford, J., Emmons, L., Kim, S., Song, C.-K., Chang, L.-S., Lee, G., Kim, J., and Park, R.: NASA Contributions to KORUS-AQ: An International Cooperative Air Quality Field Study in Korea, available on-line at https://espo.nasa.gov/home/korus-aq/content/KORUS-AQ_Science_Overview_0, 32 pages, 2015.

Anderson, T. L., and Ogren, J. A.: Determining aerosol radiative properties using the TSI 3563 integrating nephelometer, Aerosol
500   Sci. & Technol., 29:1, 57-69, doi: 10.1080/02786829808965551, 1998.

Ångström, A.: On the atmospheric transmission of sun radiation and on dust in the air (1929), in Selected papers on scattering in
the atmosphere, SPIE Milestone Series, vol. 11, edited by C. Bohren, pp. 156–166, SPIE, 1989.

505   Bluvshtein, N., Flores, J. M., Segev, L., and Rudich, Y.: A new approach for retrieving the UV-Vis optical properties of ambient
aerosols, Atmos. Meas. Tech., 9(8), 3477–3490, doi:10.5194/amt-9-3477-2016, 2016.

Bluvshtein, N., Lin, P., Flores, J. M., Segev, L., Mazar, Y., Tas, E., Snider, G., Weagle, C., Brown, S. S., Laskin, A., Rudich, Y.:
Broadband optical properties of biomass-burning aerosol and identification of brown carbon chromophores, J. Geophys. Res.-
510   Atmos., 122 (10), 5441−5456, doi:10.1002/2016JD026230, 2017.

Choi, J., Park, R. J., Lee, H. M., Lee, S., Jo, D. S., Jeong, J. I., Henze, D. K., Woo, J. H., Ban, S. J., Lee, M. D., Lim, C. S., Park,
M. K., Shin, H. J., Cho, S., Peterson, D., and Song, C. K.: Impacts of local vs. trans-boundary emissions from different sectors on
PM$_{2.5}$ exposure in South Korea during the KORUS-AQ campaign, Atmos. Environ., 203, 196–205,
515   https://doi.org/10.1016/j.atmosenv.2019.02.008, 2019.

Eck, T. F., Holben, B. N., Reid, J. S., Dubovik, O., Smirnov, A., O'Neill, N. T., Slutsker, I., and Kinne, S.: Wavelength dependence
of the optical depth of biomass burning, urban, and desert dust aerosols, J. Geophys. Res., 104:D24, 31,333–31,349, 1999.

520   Eck, T. F., Holben, B. N., Dubovik, O., Smirnov, A., Slutsker, I., Lobert, J. M., and Ramanathan, V.: Column-integrated aerosol
optical properties over the Maldives during the northeast monsoon for 1998–2000, J. Geophys. Res., 106:D22, 28,555–28,566,
2001a.

Eck, T. F., Holben, B. N., Ward, D. E., Dubovik, O., Reid, J. S., Smirnov, A., Mukelabai, M. M., Hsu, N. C., O'Neill, N. T., and
525   Slutsker, I.: Characterization of the optical properties of biomass burning aerosols in Zambia during the 1997 ZIBBEE field
campaign, J. Geophys. Res., 106:D4, 3425–3448, 2001b.

Eck, T. F., Holben, B. N., Ward, D. E., Mukelabai, M. M., Dubovik, O., Smirnov, A., Schafer, J. S., Hsu, N. C., Piketh, S. J.,
Queface, A., Le Roux, J., Swap, R. J., and Slutsker, I.: Variability of biomass burning aerosol optical characteristics in southern
530   Africa during the SAFARI 2000 dry season campaign and a comparison of single scattering albedo estimates from radiometric
measurements, J. Geophys. Res., 108:D13, 8477, doi:10.1029/ 2002JD002321, 2003a.

Eck, T. F., Holben, B. N., Ward, D. E., Mukelabai, M. M., Dubovik, O., Smirnov, A., Schafer, J. S., Hsu, N. C., Piketh, S. J.,
Queface, A., Le Roux, J., Swap, R. J., and Slutsker, I.: Correction to ''Variability of biomass burning aerosol optical characteristics
535   in southern Africa during the SAFARI 2000 dry season campaign and a comparison of single scattering albedo estimates from
radiometric measurements'' by T. F. Eck et al., J. Geophys. Res., 108:D13, 8500, doi:10.1029/2003JD001606, 2003b.

Eck, T. F., Holben, B. N., Kim, J., Beyersdorf, A. J., Choi, M., Lee, S., Koo, J. H., Giles, D. M., Schafer, J. S., Sinyuk, A., Peterson, D. A., Reid, J. S., Arola, A., Slutsker, I., Smirnov, A., Sorokin, M., Kraft, J., Crawford, J. H., Anderson, B. E., Thornhill, K. L.,

540   Diskin, G., Kim, S. W., and Park, S.: Influence of cloud, fog, and high relative humidity during pollution transport events in South Korea: aerosol properties and PM$_{2.5}$ variability, Atmos. Environ., 232, 117530, https://doi.org/10.1016/j.atmosenv.2020.117530, 2020.

Fu, G., Hasekamp, O., Rietjens, J., Smit, M., Di Noia, A., Cairns, B., Wasilewski, A., Diner, D., Seidel, F., Xu, F., Knobelspiesse,

545   K., Gao, M., da Silva, A., Burton, S., Hostetler, C., Hair, J., and Ferrare, R.: Aerosol retrievals from different polarimeters during the ACEPOL campaign using a common retrieval algorithm, Atmos. Meas. Tech., 13, 553–573, https://doi.org/10.5194/amt-13-553-2020, 2020.

Giles, D. M., Sinyuk, A., Sorokin, M. G., Schafer, J. S., Smirnov, A., Slutsker, I., Eck, T. F., Holben, B. N., Lewis, J. R., Campbell,

550   J. R., Welton, E. J., Korkin, S. V., and Lyapustin, A. I.: Advancements in the Aerosol Robotic Network (AERONET) Version 3 database – automated near-real-time quality control algorithm with improved cloud screening for Sun photometer aerosol optical depth (AOD) measurements, Atmos. Meas. Tech., 12, 169–209, https://doi.org/10.5194/amt-12-169-2019, 2019.

Hasekamp, O. P., Fu, G., Rusli, S. P., Wu, L., Di Noia, A., aan de Brugh, J., Landgraf, J., Smit, J. M., Rietjens, J., van Amerongen,

555   A.: Aerosol measurements by SPEXone on the NASA PACE mission: expected retrieval capabilities, J. Quant. Spec. & Rad. Trans., 227, 170-184, https://doi.org/10.1016/j.jqsrt.2019.02.006, 2019.

He, Q., Bluvshtein, N., Segev, L., Meidan, D., Flores, J. M., Brown, S. S., Brune, W., and Rudich, Y.: Evolution of the Complex Refractive Index of Secondary Organic Aerosols during Atmospheric Aging, Environ. Sci. Technol., 52, 3456−3465, DOI:

560   10.1021/acs.est.7b05742, 2018.

Jordan, C. E., Anderson, B. E., Beyersdorf, A. J., Corr, C. A., Dibb, J. E., Greenslade, M. E., Martin, R. F., Moore, R. H., Scheuer, E., Shook, M. A., Thornhill, K. L., Troop, D., Winstead, E. L., and Ziemba, L. D.: Spectral aerosol extinction (SpEx): a new instrument for in situ ambient aerosol extinction measurements across the UV/visible wavelength range, Atmos. Meas. Tech., 8,

565   4755–4771, doi:10.5194/amt-8-4755-2015, 2015.

Jordan, C. E., Crawford, J. H., Beyersdorf, A. J., Eck, T. F., Halliday, H. S., Nault, B. A., Chang, L.-S., Park, J., Park, R., Lee, G., Kim, H., Ahn, J-Y., Cho, S., Shin, H. J., Lee, J. H., Jung, J., Kim, D.-S., Lee, M., Lee, T., Whitehill, A., Szykman, J., Schueneman, M. K., Campuzano-Jost, P., Jimenez, J. L., DiGangi, J. P., Diskin, G. S., Anderson, B. E., Moore, R. H., Ziemba, L. D., Fenn, M.

570   A., Hair, J. W., Kuehn, R. E., Holz, R. E., Chen, G., Travis, K., Shook, M., Peterson, D. A., Lamb, K. D., and Schwarz, J. P.: Investigation of factors controlling PM$_{2.5}$ variability across the South Korean Peninsula during KORUS- AQ, Elem. Sci. Anth., 8, 28, doi:10.1525/elementa.424, 2020a.

Jordan, C. E., Stauffer, R. M., Lamb, B. T., Novak, M. Mannino, A., Crosbie, E., Schuster, G. L., Moore, R., Hudgins, C., Thornhill,

575   K. L., Winstead, E. L., Anderson, B. E., Martin, R. F., Shook, M. A., Ziemba, L. D., Beyersdorf, A. J., Robinson, C., Corr, C. A., and Tzortziou, M.: New in situ aerosol hyperspectral optical measurements over 300-700 nm, Part 2: Extinction, total absorption, water- and methanol-soluble absorption observed during the KORUS-OC cruise, *submitted to* Atmos. Chem. Phys., 2020b.

580 Kaskaoutis, D. G., Kalapureddy, M. C. R., Moorthy, K. K., Devara, P. C. S., Nastos, P. T., Kosmopoulos, P. G., and Kambezidis, H. D.: Heterogeneity in pre-monsoon aerosol types over the Arabian Sea deduced from ship-borne measurements of spectral AODs, Atmos. Chem. Phys., 10, 4893–4908, doi:10.5194/acp-10-4893-2010, 2010.

Kaskaoutis, D. G., Kharol, S. K., Sinha, P. R., Singh, R. P., Kambezidis, H. D., Sharma, A. R., and Badarinath, K. V. S.: Extremely large anthropogenic-aerosol contribution to total aerosol load over the Bay of Bengal during winter season, Atmos. Chem. Phys.,
585 11, 7097–7117, doi:10.5194/acp-11-7097-2011, 2011.

Kaufman, Y. J.: Aerosol optical thickness and atmospheric path radiance, J. Geophys. Res., 98:D2, 2677–2692, 1993.

Kim, H., Zhang, Q., and Heo, J.: Influence of intense secondary aerosol formation and long-range transport on aerosol chemistry
590 and properties in the Seoul Metropolitan Area during spring time: results from KORUS-AQ, Atmos. Chem. Phys., 18, 7149–7168, https://doi.org/10.5194/acp-18-7149-2018, 2018.

King, M. D., and Byrne, D. M.: A method for inferring total ozone content from the spectral variation of total optical depth obtained with a solar radiometer, J. Atmos. Sci., 33, 2242–2251, 1976.
595

King, M. D., Byrne, D. M., Herman, B. M., and Reagan, J. A.: Aerosol size distributions obtained by inversion of spectral optical depth measurements, J. Atmos. Sci., 35, 2153–2167, 1978.

LeBlanc, S. E., Redemann, J., Flynn, C., Pistone, K., Kacenelenbogen, M., Segal-Rosenheimer, M., Shinozuka, Y., Dunagan, S.,
600 Dahlgren, R. P., Meyer, K., Podolske, J., Howell, S. G., Freitag, S., Small-Griswold, J., Holben, B., Diamond, M., Wood, R., Formenti, P., Piketh, S., Maggs-Kölling, G., Gerber, M., and Namwoonde, A.: Above-cloud aerosol optical depth from airborne observations in the southeast Atlantic, Atmos. Chem. Phys., 20, 1565–1590, https://doi.org/10.5194/acp-20-1565-2020, 2020.

Moosmüller, H., and Chakrabarty, R. K.: Technical Note: Simple analytical relationships between Ångström coefficients of
605 aerosol extinction, scattering, absorption, and single scattering albedo, Atmos. Chem. Phys., 11, 10677–10680, doi:10.5194/acp-11-10677-2011, 2011.

Nault, B. A., Campuzano-Jost, P., Day, D. A., Schroder, J. C., Anderson, B., Beyersdorf, A. J., Blake, D. R., Brune, W. H., Choi, Y., Corr, C. A., de Gouw, J. A., Dibb, J., DiGangi, J. P., Diskin, G. S., Fried, A., Huey, L. G., Kim, M. J., Knote, C. J., Lamb, K.
610 D., Lee, T., Park, T., Pusede, S. E., Scheuer, E., Thornhill, K. L., Woo, J. H., and Jimenez, J. L.: Secondary organic aerosol production from local emissions dominates the organic aerosol budget over Seoul, South Korea, during KORUS-AQ, Atmos. Chem. Phys., 18, 17,769–17,800, https://doi.org/10.5194/acp-18-17769-2018, 2018.

O'Neill, N. T., Dubovik, O., and Eck, T. F.: Modified Ångström exponent for the characterization of submicrometer aerosols,
615 Appl. Opt., 40:15, 2368 – 2375, 2001.

Ogren, J. A., Wendell, J., Andrews, E., and Sheridan, P. J.: Continuous light absorption photometer for long-term studies, Atmos.

Meas. Tech., 10, 4805-4818, https://doi.org/10.5194/amt-10-4805-2017, 2017.

620   Peterson, D. A., Hyer, E. J., Han, S.-O., Crawford, J. H., Park, R. J., Holz, R., Kuehn, R. E., Eloranta, E., Knote, C., Jordan, C. E., and Lefer, B. L.: Meteorology influencing springtime air quality, pollution transport, and visibility in Korea, Elem. Sci. Anth., 7, 57, doi:https://doi.org/10.1525/elementa.395, 2019.

Rao, B. M., and Niranjan, K.: Optical properties of the South Asian winter haze at a tropical coastal site in India, Atmos. Environ.,
625   54, 449-455, doi:10.1016/j.atmosenv.2012.02.016, 2012.

Reid, J. S., Eck, T. F., Christopher, S. A., Hobbs, P. V., and Holben, B.: Use of the Ångstrom exponent to estimate the variability of optical and physical properties of aging smoke particles in Brazil, J. Geophys. Res., 104:D22, 27,473 – 27,489, 1999.

630   Remer, L. A., Davis, A. B., Mattoo, S., Levy, R. C., Kalashnikova, O. V., Coddington, O., Chowdhary, J., Knobelspiesse, K., Xu, X., Ahmad, Z., Boss, E., Cairns, B., Dierssen, H. M., Diner, D. J., Franz, B., Frouin, R., Gao, B.-C., Ibrahim, A., Martins, J. V., Omar, A. H., Torres, O., Xu, F., and Zhai, P.-W.: Retrieving Aerosol Characteristics From the PACE Mission, Part 1: Ocean Color Instrument, Front. Earth Sci., 7:152. doi:10.3389/feart.2019.00152, 2019a.

635   Remer, L. A., Knobelspiesse, K., Zhai, P.-W., Xu, F., Kalashnikova, O. V., Chowdhary, J., Hasekamp, O., Dubovik, O., Wu, L., Ahmad, Z., Boss, E., Cairns, B., Coddington, O., Davis, A. B., Dierssen, H. M., Diner, D. J., Franz, B., Frouin, R., Gao, B.-C., Ibrahim, A., Levy, R. C., Martins, J. V., Omar, A. H., and Torres, O. Retrieving Aerosol Characteristics From the PACE Mission, Part 2: Multi-Angle and Polarimetry, Front. Environ. Sci., 7:94. doi:10.3389/fenvs.2019.00094, 2019b.

640   Schuster, G. L., Dubovik, O., and Holben, B. N.: Angstrom exponent and bimodal aerosol size distributions, J. Geophys. Res., 111, D07207, doi:10.1029/2005JD006328, 2006.

Smit, J. M., Rietjens, J. H. H., van Harten, G., Noia, A. D., Laauwen, W., Rheingans, B. E., Diner, D. J., Cairns, B., Wasilewski, A., Knobelspiesse, K. D., Ferrare, R., and Hasekamp, O. P.: SPEX airborne spectropolarimeter calibration and performance, Appl.
645   Optics, 58, 5695–5719, https://doi.org/10.1364/AO.58.005695, 2019.

Thompson, A. M., Stauffer, R. M., Boyle, T. P., Kollonige, D. E., Miyazaki, K., Tzortziou, M., Herman, J. R., Abuhassan, N., Jordan, C. E., and Lamb, B. T.: Comparison of near surface NO_2 pollution with Pandora total column NO_2 during the Korea-United States Ocean Color (KORUS OC) Campaign, J. Geophys. Res.: Atmos., 124, 13,560-13,575,
650   https://doi.org/10.1029/2019JD030765, 2019.

Tzortziou, M., Parker, O., Lamb, B., Herman, J., Lamsal, L., Stauffer, R., and Abuhassan, N.: Atmospheric trace gas (NO_2 and O_3) variability in Korean coastal waters, implications for remote sensing of coastal ocean color dynamics, Remote Sens., 10(10), 1587; doi:10.3390/rs10101587, 2018.

655

US-Korean Steering Group: Risk reduction measurements for GEO-CAPE: A US-Korea joint field campaign (US-Korea JFC) in the East Sea and Yellow Sea, available on-line at https://geo-cape.larc.nasa.gov/pdf/KORUS_OC_WhitePaper_2016_Field_20150205_final.pdf, 18 pages, 2015.

660 Washenfelder, R. A., Flores, J. M., Brock, C. A., Brown, S. S., and Rudich, Y.: Broadband measurements of aerosol extinction in the ultraviolet spectral region, Atmos. Meas. Tech., 6, 861–877, doi:10.5194/amt-6-861-2013, 2013.

Washenfelder, R. A., Attwood, A. R., Brock, C. A., Guo, H., Xu, L., Weber, R. J., Ng, N. L., Allen, H. M., Ayres, B. R., Baumann, K., Cohen, R. C., Draper, D. C., Duffey, K. C., Edger- ton, E., Fry, J. L., Hu, W. W., Jimenez, J. L., Palm, B. B., Romer,
665 P., Stone, E. A., Wooldridge, P. J., and Brown, S. S.: Biomass burning dominates brown carbon absorption in the ru- ral southeastern United States, Geophys. Res. Lett., 42, 653–664, doi:10.1002/2014GL062444, 2015.

Werdell, P. J., Behrenfeld, M. J., Bontempi, P. S., Boss, E., Cairns, B., Davis, G. T., Franz, B. A., Gliese, U. B., Gorman, E. T., Hasekamp, O., Knobelspiesse, K. D., Mannino, A., Martins, J. V., McClain, C. R., Meister, G., and Remer, L. A.: The Plankton,
670 Aerosol, Cloud, ocean Ecosystem mission status, science, advances, BAMS, 1775-1794, doi:10.1175/BAMS-D-18-0056.1, 2019.

White, J. U.: Long optical paths of large aperture, J. Opt. Soc. Am., 32, 285–288, 1942.

675
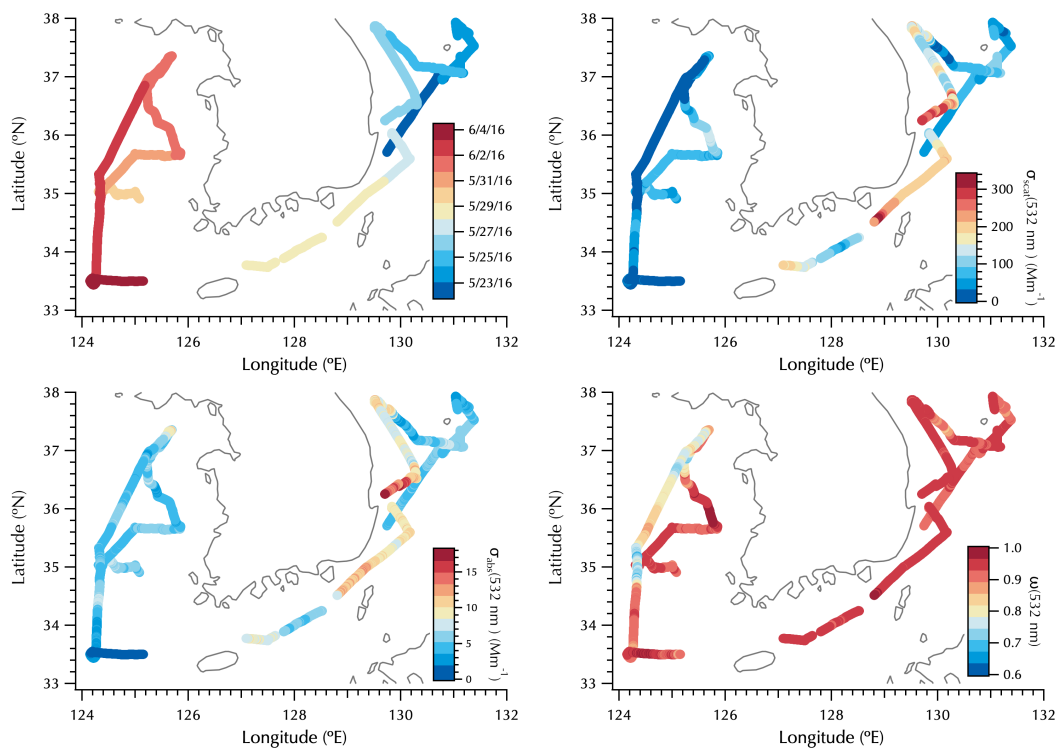
Figure 1: Cruise maps of date and time (KST, top left) with 532 nm σ_{scat} (Mm^{-1}, top right), σ_{abs} (Mm^{-1}, bottom left) and ω (bottom right).
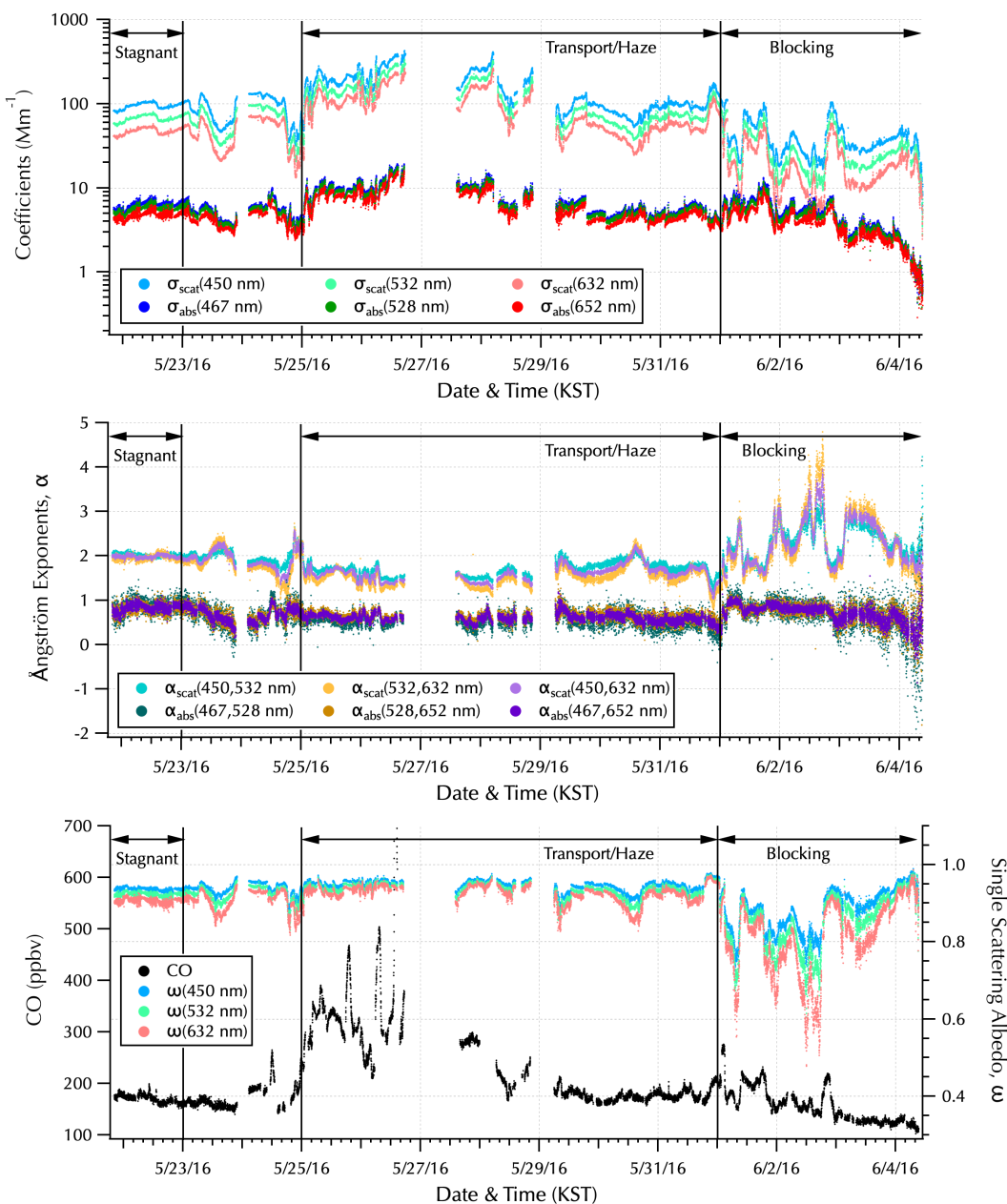
Figure 2: Top: σ_{scat} (light shades) and σ_{abs} (dark shades) averaged to 1 minute intervals during the cruise (both in units of Mm^{-1}). Middle: α_{scat} (light shades) and α_{abs} (dark shades), unitless, calculated from the wavelength pairs of the coefficients in the top panel. Bottom: ω (right axis), unitless, along with 1 minute averaged CO concentrations (ppbv). Note, the peak CO value cut off in the figure reached 1000 ppbv.

680

685
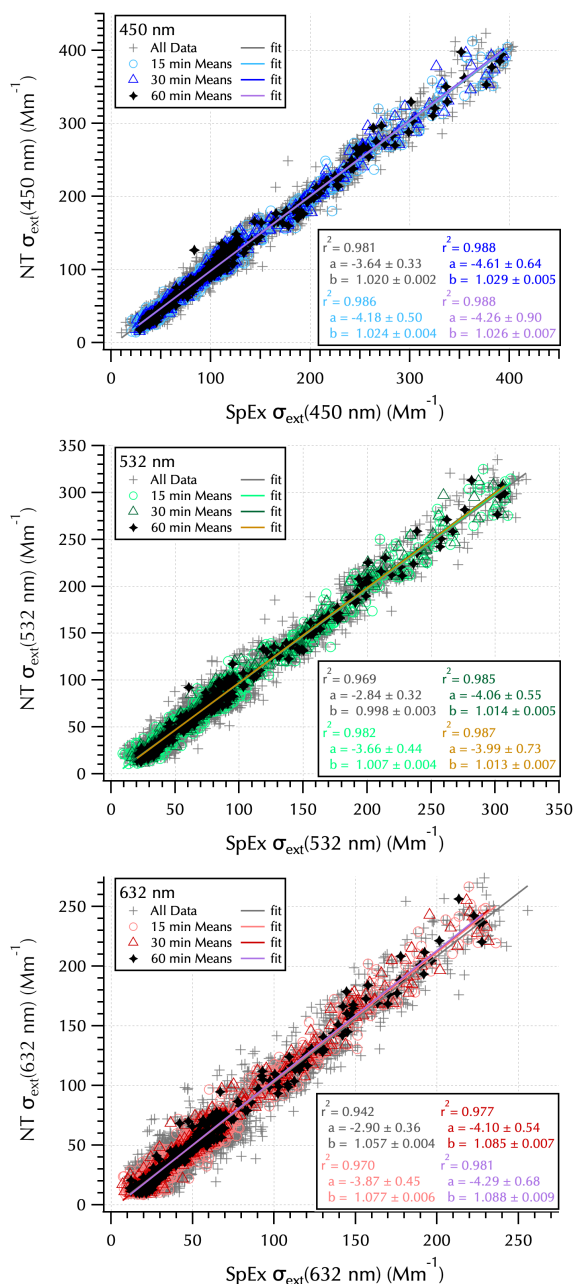
Figure 3: NT vs. SpEx σ_{ext} **(450 nm, top; 532 nm, middle; 632 nm bottom) All data points (gray pluses) are shown with 15 min (light colored circles), 30 min (dark colored triangles), and 60 min (black symbols) means. Fit lines, coefficients, and r^2 values are color-coordinated with the symbols, except for the black markers where the fit lines used a light color for visibility. Above LLOD points only.**

690
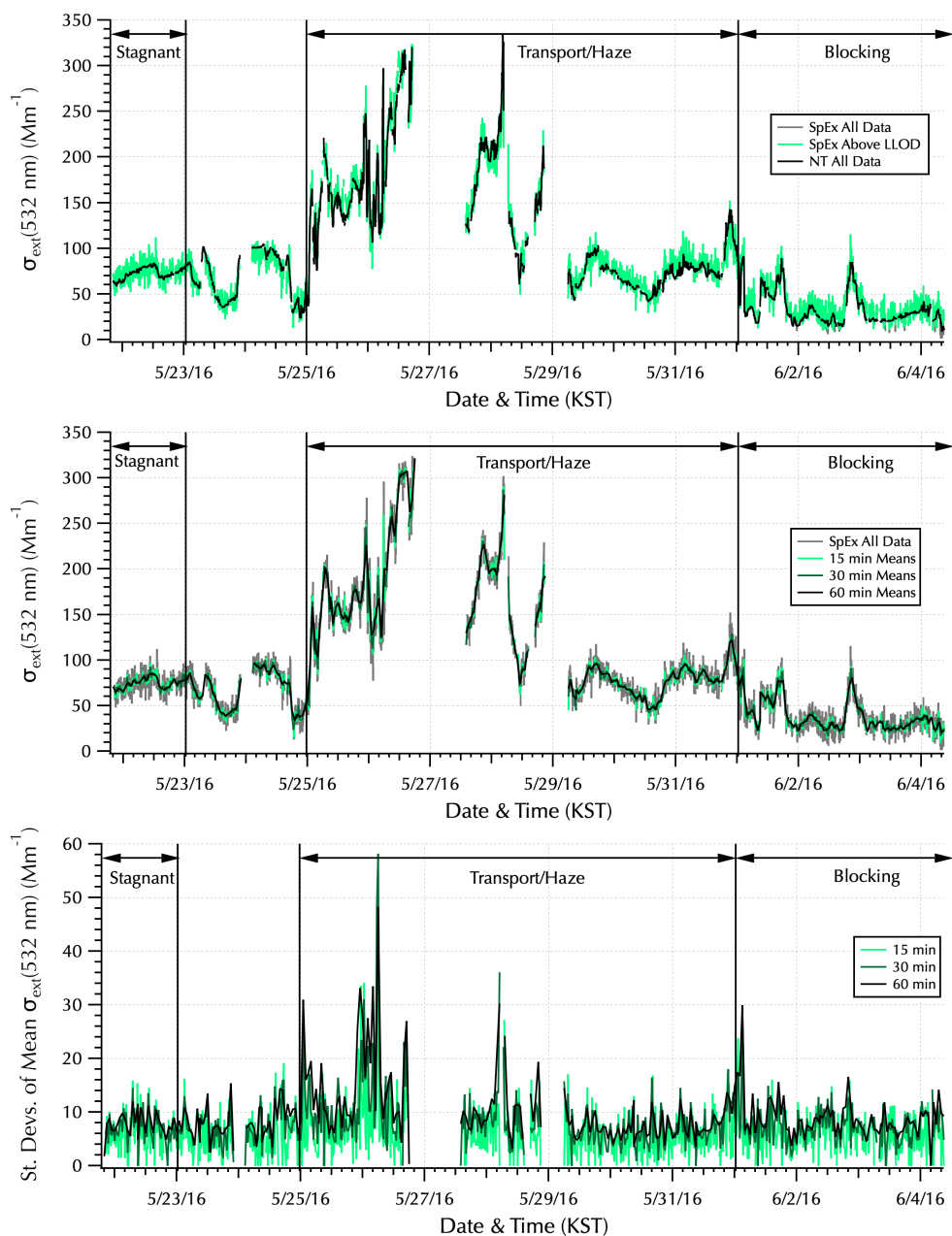
Figure 4: Time series of 532 nm σ_{ext} (Mm^{-1}) throughout the cruise. Top panel: SpEx (all data, gray; above LLOD, green; these curves are coincident until June 2nd when the lowest values are below detection and hence, appear gray) with NT σ_{ext} (black). Middle panel: SpEx (all data, gray) with 15 min (light green), 30 min (dark green), and 60 min (black) means. Bottom panel: SpEx standard deviations of the 15 min (light green), 30 min (dark green), and 60 min (black) means. Meteorological periods shown as in Fig. 2.
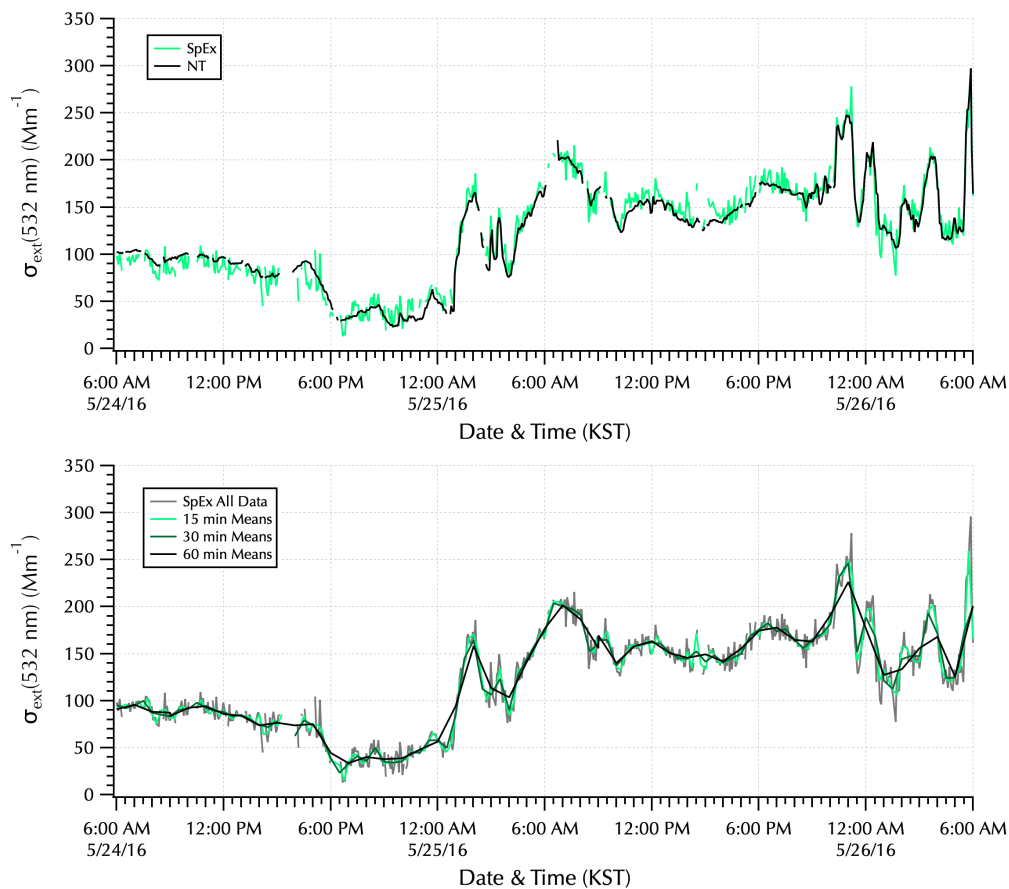
700

Figure 5: Two day highlight of the top two panels of Fig. 4. Top panel: σ_{ext}(532 nm) from SpEx (green) shown with NT (black). Bottom panel: σ_{ext}(532 nm) from SpEx (all data, gray) with 15 min (light green), 30 min (dark green), and 60 min (black) means.
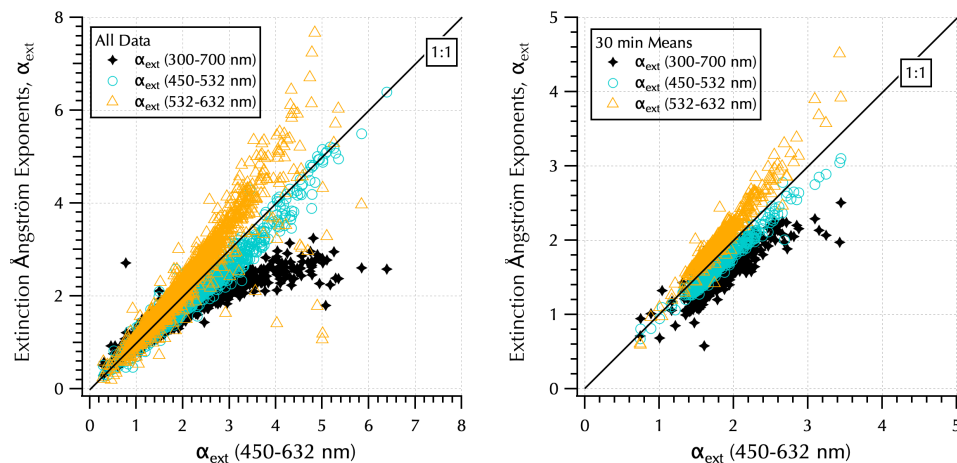
Figure 6: α_{ext} determined over 3 different wavelength ranges (300-700 nm, black diamonds, 450-532 nm, teal circles, and 532-632 nm, gold triangles) compared to that found over the 450-632 nm range (x-axis). All data (left panel) and 30 min means (right).
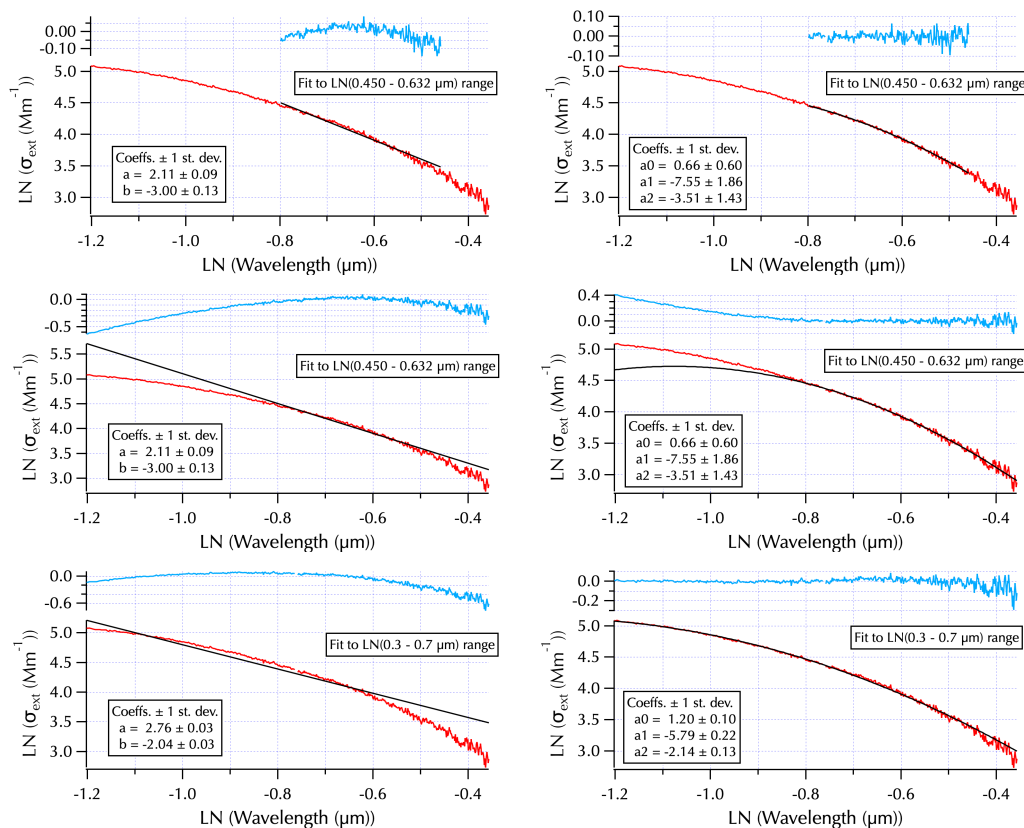
710

Figure 7. Example of wavelength dependence of LN(σ_{ext} (Mm^{-1})) spectra (red curves) as a function of LN(wavelength (μm)). Linear (y = a + b(x), left panels) and 2nd order polynomial (y = a$_0$ + a$_1$(x) + a$_2$(x^2), right panels) fits (black curves) are shown with the fit residuals (= LN(σ_{ext} (Mm^{-1})) - fit, blue curves). Residuals randomly distributed around zero indicate a good fit by the mathematical function used to fit the data, trends in residuals suggest another function may provide a better fit. Top and bottom panels show fits to a subrange

715 **(LN(0.450 - 0.632 μm)) and full range (LN(0.3 - 0.7 μm) of the measured spectrum, respectively. Middle panels show the extrapolation of the fit in the top panels over the full measured wavelength range.**
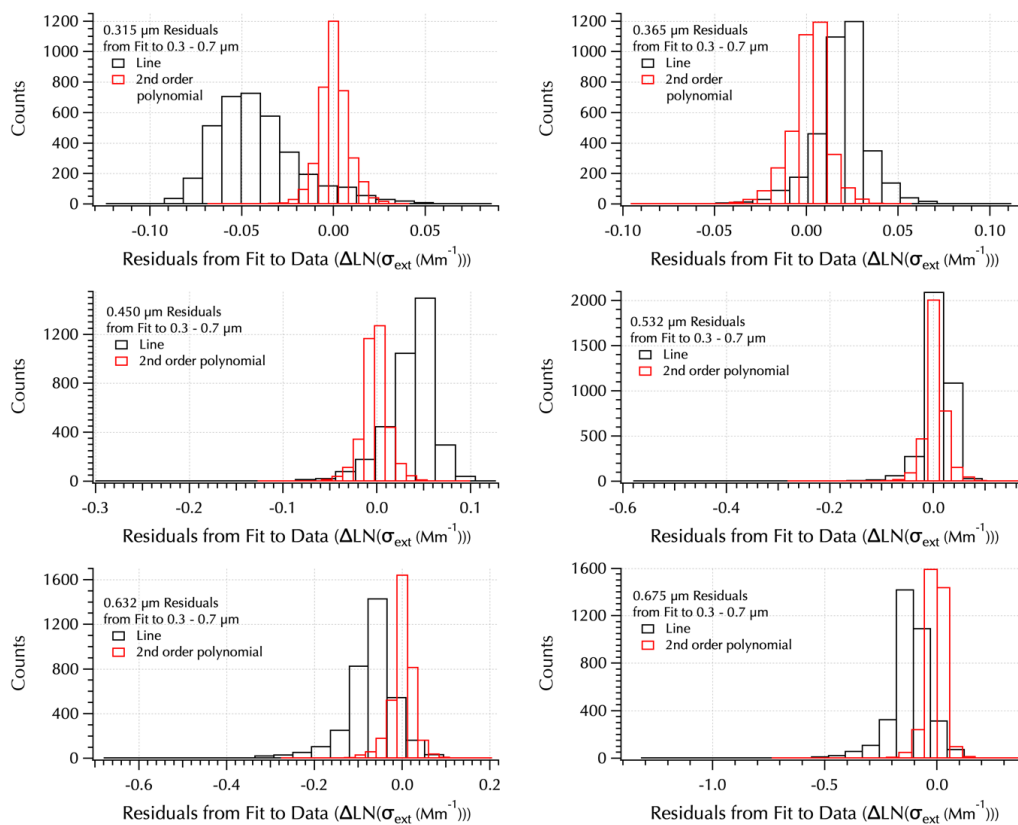
720

Figure 8: Comparison of residuals (the difference between the data and mathematical function fit to that data) from a line fit (black) and 2nd order polynomial fit (red) to the measured LN(σ_{ext}(Mm^{-1})) spectra over the 0.3 - 0.7 μm range for 6 wavelengths: 0.315 (top left), 0.365 (top right), 0.45 (middle left), 0.532 (middle right), 0.632 (bottom left), and 0.675 μm (bottom right).
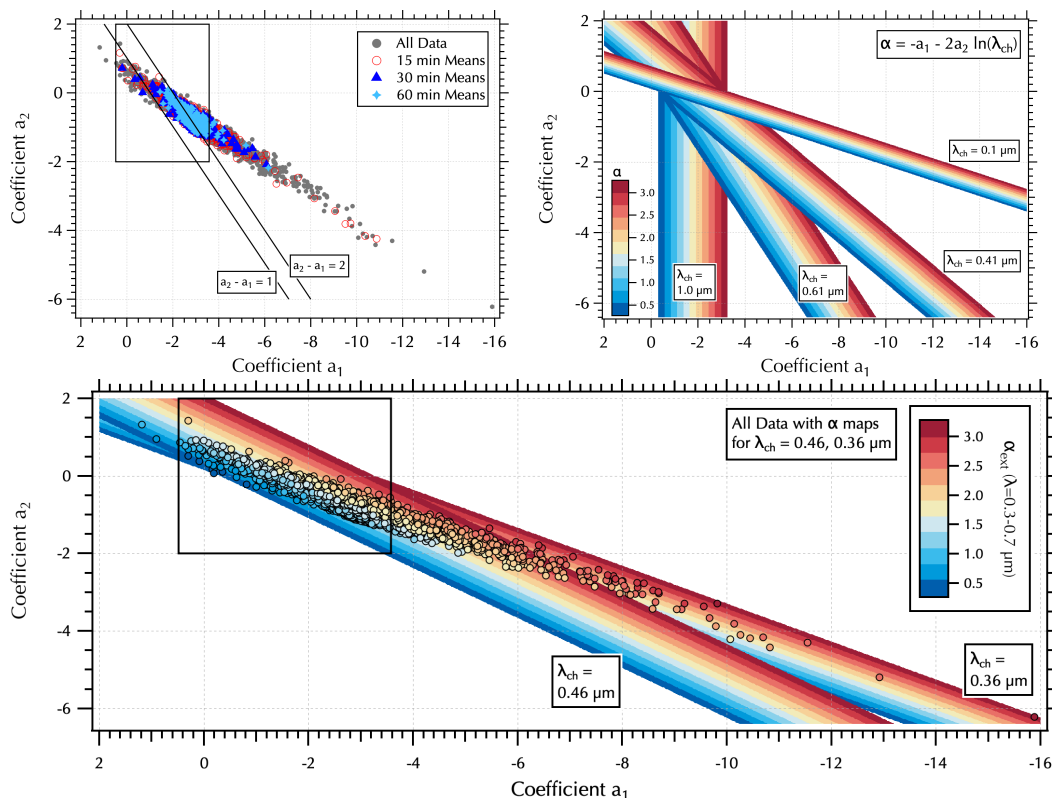
Figure 9: Top left: coefficients a_2 versus a_1 from 2nd order polynomial fits to the full wavelength range (0.3 - 0.7 µm) of the individual (All Data, gray filled circles) and mean (15 min, red open circles, 30 min, dark blue triangles, and 60 min, light blue diamonds, average) spectra. Black box shows the limits of the Schuster et al. [2006] Fig. 6 plot, black lines show approximate equivalents to $\alpha_{ext} = 1$ and 2 from that work. Top right: α mapped into (a_1,a_2) space as a function of the characteristic wavelength (λ_{ch}) of the measured spectral range. Bottom: α_{ext} calculated from the full spectral range of SpEx (colored dots) overlaid on α maps that cover the range of λ_{ch} values calculated from the data set.
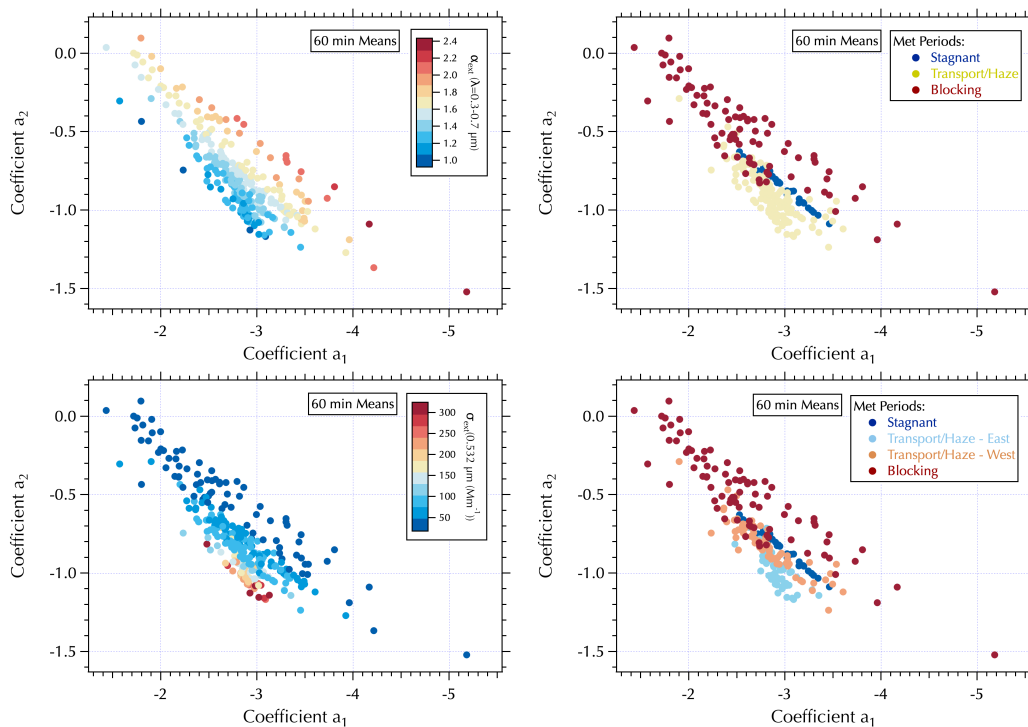
735

Figure 10: Coefficients a_2 vs. a_1 from 2nd order polynomial fits to the full wavelength range (0.3-0.7 µm) of the 60 min mean spectra colored by α_{ext} (λ=0.3-0.7 µm), top left, σ_{ext} (0.532 µm (Mm^{-1})), bottom left, and the defined meteorological periods described in Peterson et al. [2019], top right (i.e., excluding the interval when the meteorological regime was in transition, May 23rd and 24th, and hence, undefined). The bottom right panel is the same as the top right, but with the Transport/Haze samples split between those measured to

740 **the east (May 25th-27th) and west (May 29th-31st) of the peninsula, excluding those samples collected in transit between the two.**